

# *Hubble Space Telescope Imaging in the Chandra Deep Field South:* **III. Quantitative Morphology of the 1 Million Second Chandra Counterparts and Comparison with the Field Population**<sup>1</sup>

N. A. Grogin<sup>1</sup>, A. M. Koekemoer<sup>2</sup>, E. J. Schreier<sup>2,3</sup>, J. Bergeron<sup>4</sup>, R. Giacconi<sup>1,3</sup>,  
G. Hasinger<sup>5</sup>, L. Kewley<sup>6</sup>, C. Norman<sup>1</sup>, P. Rosati<sup>4</sup>, P. Tozzi<sup>7</sup>, and A. Zirm<sup>1</sup>

## ABSTRACT

We present quantitative morphological analyses of 37 *HST*/WFPC2 counterparts of X-ray sources in the 1 Ms Chandra Deep Field–South (CDFS). We investigate: 1) one-dimensional surface brightness profiles via isophotal ellipse fitting; 2) two-dimensional, PSF-convolved, bulge+disk+nucleus profile-fitting; 3) asymmetry and concentration indices compared with all  $\sim 3000$  sources in our three WFPC2 fields; and 4) near-neighbor analyses comparing local environments of X-ray sources versus the field control sample. Significant nuclear point-source optical components appear in roughly half of the resolved *HST*/WFPC2 counterparts, showing a narrow range of  $F_X/F_{opt,nuc}$  consistent with the several *HST*-unresolved X-ray sources (putative type 1 active galactic nuclei [AGNs]) in our fields. We infer roughly half of the *HST*/WFPC2 counterparts host unobscured AGN, comparable to analogous low-redshift AGN samples and suggesting no steep decline in the type 1/type 2 ratio out to the redshifts  $z \sim 0.5 - 1$  typical of our sources. The concentration indices of the CDFS counterparts are clearly larger on average than those of the field distribution, at 5-sigma, suggesting that

---

<sup>1</sup>Department of Physics and Astronomy, Johns Hopkins University, Baltimore, MD 21218, USA

<sup>2</sup>Space Telescope Science Institute, 3700 San Martin Drive, Baltimore, MD 21218, USA

<sup>3</sup>Associated Universities, Inc., 1400 16th Street NW, Washington, DC 20036, USA

<sup>4</sup>European Southern Observatory, Karl-Schwarzschild-Strasse 2, Garching, D-85748, Germany

<sup>5</sup>Max-Planck-Institut Für extraterrestrische Physik, Giessenbachstrasse PF 1312, Garching D-85748, Germany

<sup>6</sup>Harvard-Smithsonian Center for Astrophysics, 60 Garden St., Cambridge, MA 02138, USA

<sup>7</sup>Osservatorio Astronomico di Trieste, Via G. B. Tiepolo 11, 34131 Trieste, Italy

the strong correlation between central black hole mass and host galaxy properties (including concentration index) observed in nearby galaxies is already evident by  $z \sim 0.5 - 1$ . By contrast, the asymmetry index distribution of the 21 resolved CDFS sources at  $I < 23$  is indistinguishable from the  $I < 23$  field. Moreover, the frequency of  $I < 23$  near neighbors around the CDFS counterparts is not significantly different from the field sample. These results, combined with previous similar findings for local samples, suggest that recent merger/interaction history is not a good indicator of AGN activity over a substantial range of look-back time.

*Subject headings:* galaxies: structure — X-rays: galaxies — galaxies: active — galaxies: fundamental parameters — surveys

## 1. Introduction

It is becoming clear that a proper understanding of galaxy formation and evolution must address the role played by the supermassive black holes (SBH) now suspected to be present in most galaxy nuclei (e.g., Magorrian et al. 1998) and responsible for the AGN phenomenon. In the local universe, the importance of the SBH–host-galaxy relationship has been highlighted recently by the tight correlation of SBH mass with the host bulge velocity dispersion (Gebhardt et al. 2000; Ferrarese & Merritt 2000) and concentration index (Graham et al. 2001). It is of great interest to probe the AGN–host-galaxy relationship out to higher redshifts, where, for example, the strong evolution observed at the low end of the AGN luminosity function by *ROSAT* deep X-ray surveys (Hasinger et al. 1999; Miyaji et al. 2000) has been associated with an increased rate of galaxy interactions and distorted/irregular morphologies in the early universe (Lilly et al. 1998; Abraham et al. 1999).

The recent *Chandra X-ray Observatory* (*CXO*) Deepest Field surveys have extended the *ROSAT* results to fainter fluxes and harder X-ray energies (Cowie et al. 2003; Giacconi et al. 2002; Brandt et al. 2001; Hornschemeier et al. 2001; Mushotzky et al. 2000; Tozzi et al. 2001). These studies have also confirmed that the cosmic X-ray background is largely attributable to moderate-luminosity AGN ( $L_X \sim 10^{43-44}$  erg s $^{-1}$ ) at moderate to high redshifts ( $z \gtrsim 0.5$ ), many with significant obscuration by the host galaxy. This underscores the desirability of studying the AGN–host connection with samples detected at hard X-ray

---

<sup>1</sup>Based on observations made with the NASA/ESA Hubble Space Telescope, which is operated by the Association of Universities for Research in Astronomy, Inc., under NASA contract NAS 5-26555.

energies, where there is much less bias against the dust obscuration that segregates AGN into type 1 (unobscured) and type 2 (obscured) in the standard unified model (e.g., Urry & Padovani 1995). Although much has been learned from studies of AGN and their hosts at low redshift, and from comparisons of the evolution of higher-luminosity AGN and field galaxies at high redshifts, the fundamental question of whether nuclear activity drives galaxy evolution, or vice versa, can only be fully addressed by obtaining high-resolution multi-wavelength observations of *typical* AGN and their hosts over a *wide range* of redshifts. The combination of *Hubble Space Telescope* (*HST*) and *CXO* deep imaging offers a unique opportunity to satisfy these requirements: the *Chandra* Deepest Fields contain the requisite large, unbiased sample of distant low- to moderate-luminosity AGN with the high positional accuracy ( $\lesssim 0''.5$ ) necessary for unambiguous association with their faint host galaxies; subsequent high-resolution *HST* images of these regions then permit the detailed investigation of their host galaxy morphologies and environments.

To this end, we obtained the first *HST* imaging within the *Chandra* Deep Field South (hereafter CDFS; Giacconi et al. 2002): three moderately-deep exposures using the Wide Field Planetary Camera 2 (WFPC2) in *V* and *I*. In Paper I of this series (Schreier et al. 2001), we identified unambiguous *HST* counterparts for  $> 90\%$  of the 26 CDFS sources in the initial 300 ksec exposure (Tozzi et al. 2001), and discussed the heterogeneous nature of this population as indicated by the joint X-ray and optical photometry. Paper II (Koekemoer et al. 2002) extended this analysis to the larger population of 40 CDFS sources revealed at the 1 Ms *CXO* depth, which is still current at the time of this writing. Again we found a  $> 90\%$  fraction with unambiguous *HST* counterparts, and the combined X-ray and optical properties of this expanded sample largely reinforced the conclusions of Paper I: the optical counterparts to the X-ray sources are divided into two distinct populations, namely 1) an optically faint group with relatively blue colors, similar to the faint blue field galaxy population, and 2) an optically brighter group, including resolved galaxies with average colors significantly redder than the corresponding bright field galaxy population. The brighter objects comprise a wide range of types, including early and late type galaxies, starbursts, and AGN, most at moderate redshifts ( $z \sim 0.4\text{--}1.0$ ; Szokoly et al., in prep.). The faint blue X-ray population is consistent with expected numbers and characteristics of low- to moderate-luminosity type 2 AGN at the quasar epoch ( $z \sim 2\text{--}3$ ).

In the present paper, we undertake a detailed morphological analysis of the CDFS optical counterparts introduced in Papers I and II. In §2 we review the *HST* and *CXO* imaging of the CDFS, introduce the full *HST*/WFPC2 source list, and review the matching of sources common to both sets of observations. We then present a variety of morphological analyses of the *HST* data in §3, including isophotal ellipse fitting and point-spread function (PSF) convolved two-dimensional surface-brightness modeling of the *CXO* counterparts, as well as

determinations of asymmetry and concentration indices for the entire *HST* source list in order to contrast the *CXO* counterparts with the much more numerous field population in our WFPC2 frames. We discuss the implications of these findings in §4 and conclude in §5. Throughout this paper we adopt a cosmology with  $\Omega_M = 0.3$ ,  $\Omega_\Lambda = 0.7$ , and  $H_0 = 70 \text{ km s}^{-1} \text{ Mpc}^{-1}$ .

## 2. Observations and Source Catalogs

In §2.1 and §2.2 we provide a brief summary of the *HST* and *CXO* observations used in this study. We refer the reader to Paper II and to Giacconi et al. (2002), respectively, for detailed descriptions of the *HST* and *CXO* observations and reduction. In §2.3 we present the combined source catalog from our three *HST*/WFPC2 fields and summarize the optical–X-ray source matching procedure detailed in Paper II. We conclude this section with the catalog of 37 optical–X-ray associations in these fields, whose *HST* morphologies and environments we analyse in the following sections.

### 2.1. *HST* Observations and Reduction

We observed three *HST*/WFPC2 fields within the CDFS during the period 22–27 July 2000. Each field received 3700s ( $\sim 2$  orbits) exposure in the F606W filter and 5800s ( $\sim 3$  orbits) in the F814W filter. In each filter the exposure time was divided among four pairs of images, arranged in a compact dither pattern with sub-pixel offsets to ameliorate the undersampled *HST* PSF of the  $0''.1/\text{pixel}$  Wide-Field (WF) cameras. We refer the reader to Tables 1 and 3 of Paper II for the specific field coordinates and observation log.

After retrieving the images from the *HST* Data Archive, we re-calibrated them through the standard pipeline once the most up-to-date calibration reference files for the time of the observations became available. We next registered each set of eight images corresponding to a given field and filter combination via cross-correlation, using tasks in the IRAF/STSDAS *dither* package. To take advantage of our sub-pixel dithering, we employed the *drizzle* software (Fruchter & Hook 2001) to combine the images with cosmic-ray rejection onto a  $0''.05/\text{pixel}$  grid (half the WF scale) with a `pixfrac` parameter of 1.0. These drizzled images are shown in Figure 1 of Paper I. The image combination is described in more detail in Paper II.

The zeropoints of the stacked images are  $ZP(F606W) = 33.322$  and  $ZP(F814W) = 32.084$  in the VEGAMAG system, which we adopt throughout this paper when quoting

magnitudes or surface brightnesses. The background noise RMS in the WF portions of the images is  $\approx 3.1$  ADU in both F606W and F814W, and in the PC portions is  $\approx 8.2$  ADU in F606W and  $\approx 8.6$  ADU in F814W. For notational convenience, we refer to measurements from the F814W images as “*I*” and from the F606W images as “*V*”, though we note that the F606W passband is significantly broader and redder than Johnson *V*.

## 2.2. CXO Observations

The CDFS (Giacconi et al. 2002, Rosati et al. 2002) comprises a set of 11 *CXO*/ACIS-I exposures totaling 942 ksec, taken between October 1999 and December 2000 with varying position angle, and centered at  $\alpha = 03^{\text{h}}32^{\text{m}}28^{\text{s}}$ ,  $\delta = -27^{\circ}48'30''$  (J2000) in a region of low Galactic neutral hydrogen column ( $N_{\text{HI}} \sim 8 \times 10^{19} \text{ cm}^{-2}$ ) and devoid of bright stars ( $m_V \leq 14$ ) within  $30'$ . The stacked CDFS image covers  $0.109 \text{ deg}^2$  and has  $\sim 1''$  resolution near the aimpoint, where the flux limits reach  $5.5 \times 10^{-17} \text{ ergs s}^{-1} \text{ cm}^{-2}$  in the soft band (0.5–2 keV) and  $4.5 \times 10^{-16} \text{ ergs s}^{-1} \text{ cm}^{-2}$  in the hard band (2–10 keV). The CDFS team has identified 346 high-significance point sources across their stacked 1 Ms image (Giacconi et al. 2002), of which 40 fall within the three *HST*/WFPC2 fields in this study —  $\approx 3$  times the number of Chandra Deep Field North sources appearing in the Hubble Deep Field–North (Brandt et al. 2001). The overdensity of CDFS sources in our three fields is partly by construction, as we chose the WFPC2 aimpoints for a large overlap with the earlier CDFS 300 ksec source list (Tozzi et al. 2001).

## 2.3. WFPC2 Photometry and Source Association

Following the reduction described in Paper I, we used SExtractor (version 2.2.1; Bertin & Arnouts 1996) in multiple-image mode to detect sources from the stacked *V+I* WFPC2 images and perform photometry of these sources on the *V* and *I* frames. Table 1 is the source catalog produced from the *HST* data, containing all sources detected in the three WFPC2 fields of view, according to the detection criteria discussed in Paper I. The catalog is complete to  $I \sim 26.4$  and  $V \sim 27.6$ . In addition to the J2000 coordinates and *V* and *I* magnitudes (SExtractor MAG\_AUTO), we include the SExtractor determinations of half-light radius,  $r_{0.5}$ , and stellarity measure,  $\eta$ , defined such that  $\eta \rightarrow 1$  for an unresolved surface-brightness profile and  $\eta \rightarrow 0$  for a resolved profile. We further include each source’s asymmetry (*A*) and concentration (*C*) indices, to be discussed in §3.3.

We registered each of the three fields independently to the CDFS frame by subtracting

the error-weighted median offset of the nearest *HST*/WFPC2 optical counterpart to each *CXO* source, typically  $\sim 1''$ . After this registration, the RMS of the optical/X-ray offsets is  $\approx 0''.5$ , consistent with the *CXO* positional uncertainties (Tozzi et al. 2001). Table 2 lists the 37 X-ray sources found by Giacconi et al. (2002) in the 1 Ms CDFS that were also detected in our WFPC2 observations. We do not list the three additional Giacconi et al. sources in our WFPC2 fields for which we did not detect an optical counterpart within  $2''$  (see Paper II). Table 2 includes the Giacconi et al. catalog XID number, IAU-format coordinate designation, hard-band (2–10 keV) X-ray flux, and X-ray hardness ratio, defined as  $(H - S)/(H + S)$  where  $H$  and  $S$  are the measured counts in the hard and soft (0.5–2 keV) bands, respectively. For convenience, we repeat from Table 1 the  $V$  and  $I$  magnitudes and stellarities, and the  $I$ -band half-light radius, concentration index, and asymmetry index. We also tabulate the nuclear-to-total flux ratio, to be discussed in §3.2.

### 3. Morphological Analyses

We performed a number of quantitative analyses of the morphology of the optical galaxies associated with the CDFS X-ray sources. For the brighter resolved sources ( $I < 24$ ,  $\eta_V < 0.5$ ), we carried out isophotal fitting (§3.1) and two-dimensional model fitting (§3.2). For all the WFPC2 sources, including those not seen in X-rays, we also measured the asymmetry and concentration indices (§3.3), following the techniques of Conselice, Bershady, & Jangren (2000) and Bershady, Jangren, & Conselice (2000, hereafter BJC00).

#### 3.1. Isophote Fitting

We fit surface brightness profiles with the IRAF isophotal analysis package ISOPHOTE, part of STSDAS. The package’s contour fitting task *ellipse* works from an initial guess for an isophotal ellipse, then steps logarithmically in major axis. At each step it finds the optimal isophotal ellipse center, ellipticity, and positional angle. Prior to the ellipse fitting, we use the task *imedit* to mask foreground stars, neighboring galaxies, etc., near the galaxies of interest. Such masked pixels are ignored by *ellipse*. We first construct the  $V$ -band surface brightness profile, then apply those isophotes to the corresponding  $I$ -band image to obtain isophotal colors.

Because the *ellipse* algorithm averages pixels within an elliptical annulus, it is capable of fitting isophotes out to a surface brightness  $\mu_V \approx 25.7$  mag arcsec $^{-2}$ , well below the RMS noise. Far enough from the galaxy center, the fitting algorithm will ultimately fail to

converge, and *ellipse* enters a non-fitting mode that fixes larger ellipses to be similar to the largest convergent isophote. We generally ran *ellipse* non-interactively, but in cases where a peculiar galaxy surface brightness profile sent the task into non-fitting mode prematurely, we stepped through the isophote fitting interactively. We show the resulting surface brightness profiles in Figure 1, also including the isophotal color, position angle, and ellipticity as a function of semimajor axis. We have fit the one-dimensional profiles to bulge/disk models using the IRAF task *nfit1d* to assist in our classification of the optical morphologies (Paper II).

### 3.2. Two-dimensional Profile Fitting

We have fit parametric two-dimensional surface brightness models combining an exponential disk, an  $R^{1/4}$  bulge, and a point-source nucleus all constrained to a common center. The parameters of the fit are the disk scale-length  $R_d$ , inclination  $i_d$ , and position angle  $PA_d$ , the bulge effective radius  $R_b$ , ellipticity  $\epsilon_b$ , and position angle  $PA_b$ , the bulge-to-disk flux ratio  $B/D$ , the point-source to total flux ratio  $P/T$ , the total source flux  $T \equiv (B + D + P)$ , the coordinates of the profile center, and a uniform background level. We pixellize the intensity distribution given by the above 12 parameters to the same scale as the data ( $0''.05/\text{pixel}$ ), using a 3 times oversampled grid in the central  $11 \times 11$  pixels to maintain accuracy in the presence of steep intensity gradients.

We convolve this model-predicted source image by the WFPC2 PSF at the location of the source. Because there are too few point sources in our images to reliably map the spatially variable WFPC2 PSF with our data, we estimate the PSF appropriate to each *CXO* counterpart with the help of the Tiny Tim software (v6.0, Krist & Hook 2001). We first generate a 4 times oversampled WFPC2 PSF image with Tiny Tim, which we then convolve with the WFPC2 pixel response function (Gaussian with  $\sigma = 0.28$  pixel; A. Fruchter 2003, private comm.) as this is not automatically done by Tiny Tim for oversampled PSFs. We simulate the effect on the PSF of drizzling with *pixfrac*=1.0 onto a  $0''.05/\text{pixel}$  grid by further convolving the oversampled PSF image with the input ( $0''.1$ ) and output ( $0''.05$ ) pixels. Finally, we block-average the oversampled PSF up to the desired  $0''.05 \text{ pixel}^{-1}$  scale.

We fit the PSF-convolved model to an image section centered on the source coordinates and extending well beyond the faintest detectable isophote: as small as  $64 \times 64$  pixels ( $3''.2$  square) for the  $I \gtrsim 22$  sources, and as large as  $256 \times 256$  pixels ( $12''.8$  square) for the  $I \approx 18$  edge-on spiral CDFS J033208.6–274649. As with the isophote fitting described in §3.1, we mask out neighboring sources, chip edges, etc., and ignore such masked pixels when calculating the goodness of fit. We derive a noise image in this region from the data itself,

assuming Poisson statistics. We calculate a figure-of-merit  $\chi^2(\mathbf{p})$  for a given parameter set  $\mathbf{p}$  by subtracting the model image from the data, dividing this difference image by the noise image, and summing the squares of the resulting pixel values. This algorithm neglects the small-scale noise correlation introduced into the data by our drizzling procedure, but we expect the effect to be minimal (see also Casertano et al. 2000).

We implement the parameter fitting in IDL, using as inputs: the data image section; the associated RMS noise image; and the PSF image. The fitting proceeds in two stages, starting with a downhill simplex optimization of  $\chi^2(\mathbf{p})$  based on the “amoeba” subroutine from Numerical Recipes (Press et al. 1992). In order to minimize our sensitivity to starting values in the optimization, we seed the initial simplex with randomly-generated parameter values spanning the broadest range in the various parameters. In the second stage of the fitting, we try to improve upon the local minimum found in the first stage by using the best-fit parameters as one of the starting points for a further simulated-annealing simplex optimization based on the “amebsa” subroutine from Numerical Recipes (Press et al. 1992).

We extensively tested the fidelity of the model-fitting code with simulated galaxy images matched to the PSF and noise properties of our data, with representative fluxes ( $10^3$ – $10^5$  counts:  $19.6 < I < 24.6$ ) and scale lengths (3–10 pixels:  $0''.15$ – $0''.5$ ), and spanning the full ranges of profile shape parameters. We found that the code performed very well at recovering  $P/T$  and moderately well at recovering  $B/D$  for simulated galaxies with  $\gtrsim 10^4$  counts ( $I \lesssim 22.1$ ). For example, the code typically recovered  $P$  in simulated  $I = 22.1$  galaxies to within 10% over the full range of  $P/T$ , and for  $P = 0$  models it typically returned  $3\sigma$  upper limits of  $P/T \lesssim 1\%$  ( $I \gtrsim 27.1$ ). For fainter simulated galaxies of  $10^3$  counts ( $I = 24.6$ ), the signal-to-noise became too poor for adequate model fits. We therefore restrict our discussion of the two-dimensional profile-fitting results to the  $I < 23$  galaxies in our sample, where in particular we have high confidence in the central point-source recovery.

To determine the uncertainty in the best-fit value for the central point-source flux  $P$ , we first define the PSF-weighted chi-square of the best-fit parameter set:  $\chi_{\text{PSF}}^2 \equiv \sum_{\text{pixels}} \text{PSF}_i \chi_i^2(\mathbf{p}_{\text{best}})$ . Starting from the best-fit point-source flux  $P_{\text{best}}$ , we step away from this value with increasing  $\Delta P$ , at each step carrying out a downhill simplex minimization of all the parameters subject to the constraint  $T \times (P/T) = (P_{\text{best}} + \Delta P)$ . We continue to increase  $\Delta P$  in both directions until reaching the effective  $3\sigma$  perturbations,  $\Delta P_{3\sigma}$ , defined according to  $\chi_i^2[\mathbf{p}; P = (P_{\text{best}} + \Delta P_{3\sigma})] = \chi_i^2(\mathbf{p}_{\text{best}}) + 9\chi_{\text{PSF}}^2$ . We have adopted this more conservative approach to estimating the errors on the point-source component because the  $\chi^2/\text{pixel}$  in the immediate vicinity of the galaxy core is often much larger than the mean  $\chi^2/\text{pixel}$  across the entire comparison region. If this procedure indicates that  $P = 0$  is not excluded at  $> 3\sigma$ , we quote a  $3\sigma$  upper-limit to the galaxy’s point-source component in Table 2. Otherwise we

quote  $P_{\text{best}}$  with its  $\pm 1\sigma$  errors.

### 3.3. Asymmetry and Concentration Indices

We measure an asymmetry index  $A$  of all WFPC2 sources (both X-ray counterparts and X-ray undetected field sources) in the three fields following the prescription of Conselice et al. (2000), which we summarize here. For each source, we determine its half-light radius  $r_{0.5}$  using SExtractor. We then extract the square image section  $S$  centered on the source with sides of length  $6 r_{0.5}$ . We rotate  $S$  by  $180^\circ$  to obtain the comparison image  $S_{180}$ . The asymmetry index is then calculated according to the formula

$$A = \min \left( \sum_{\text{pix}} |S - S_{180}| / \sum_{\text{pix}} |S| \right) - A_0,$$

where the summation is over individual pixels, and the minimization is over a fractional-pixel grid (with spacing of 0.2 pixel, or  $0'.01$ ) of possible centers of rotation. We determine the asymmetry zeropoint  $A_0 = \min \left( \sum_{\text{pix}} |B - B_{180}| / \sum_{\text{pix}} |B| \right)$  from a fixed large square region  $B$  of blank sky on the particular chip where the source resides. Because the background noise properties vary between pointings and between the WFs and the PC, we cannot simply use a single  $A_0$  for all sources.

Sources which happen to fall close to a chip edge, or happen to have a spurious companion very close in projection, will have artificially inflated asymmetry estimates in this prescription. We have modified the asymmetry index code (in IRAF, provided to us by C. Conselice) to correct for the former bias by masking the regions along chip edges where the exposure map falls off. When a source’s image section  $S$  contains such masked pixels, we exclude those pixels (and their  $180^\circ$ -rotated counterparts) from the summation above. Fortunately, this chip-edge asymmetry inflation affects only a small fraction of all sources (e.g., two of 37 *CXO* counterparts: CDFS XIDs 185 and 538), and should not introduce a bias between the asymmetry distributions of *CXO* and non-*CXO* sources. We do not attempt to correct the “spurious-companion” bias, because we do not know *a priori* if two neighboring sources are only close because of projection. As with the chip-edge bias, we do not expect the spurious-companion bias to preferentially affect either *CXO* or non-*CXO* sources.

We list the *I*-band asymmetry indices of all field sources in Table 1, and list the asymmetries with associated errors (as computed by the Conselice code) for the *CXO* counterparts in Table 2. We flag with colons the asymmetry indices in Table 2 which are suspect (anomalously large) because of substantial source overlap with a chip boundary (CDFS XIDs 185 and 538) or likely spurious close neighbor (CDFS XID 36). We plot the asymmetries of all

sources versus magnitude in Figure 2, denoting the *CXO* counterparts by large symbols keyed to morphological type as classified in Paper II: E/S0 (circles); S/Irr (squares); unresolved (stars); and indeterminate (triangles). We also plot the median  $A$  and median uncertainty in  $A$  for field sources in successive 1-mag bins (crosses with error bars). We see no significant trend in  $A$  with magnitude, but the typical measurement error becomes substantial ( $\gtrsim 0.1$ ) by  $I \approx 23$ . We therefore restrict our samples to  $I < 23$  when discussing the implications of the asymmetry measurements in §4.3.

We measure the concentration index  $C$  of all sources in the three fields following the prescription of BJC00. Using SExtractor to measure the radii containing 20% and 80% of each source’s flux ( $r_{0.2}$  and  $r_{0.8}$ , respectively), we then compute the concentration index as  $C \equiv 5 \log(r_{0.8}/r_{0.2})$ . Given this definition, a pure exponential profile has  $C = 2.80$ , while a pure  $R^{1/4}$  profile has  $C = 5.27$ . A Gaussian profile has  $C = 2.15$ , and thus an observed PSF-convolved exponential or  $R^{1/4}$  profile will appear less concentrated than the theoretical values. We list the concentration indices for the individual *CXO* counterparts in Table 2 and plot the distribution of concentration with magnitude in Figure 3 for both the X-ray counterparts (large symbols) and all the sources in the field (small symbols). We note that the high-asymmetry galaxy CDFSJ033211.0–274343 ( $A = 0.47$ ), which is significantly truncated by a chip edge, is the lone low-concentration outlier among the brighter *CXO*-detected sources.

Because the SExtractor detection algorithm requires a minimum number of connected pixels above a minimum counts/pixel threshold, sources at the faintest flux levels will be preferentially detected if they have a flatter intensity profile. This detection bias should be reflected in a systematic decline of the mean  $C$  at the faintest flux levels, which we indeed observe in Figure 3 at  $I \gtrsim 23$ –24. When discussing the implications of the concentration measurements in §4.5, we avoid the complications of this detection bias by restricting our analysis to the  $I < 24$  population.

We estimate the error on  $C$  because of uncertainty in the total flux of the source by measuring the additional two flux-radius ratios  $C_{\pm} \equiv 5 \log(r_{0.8(1\pm\sigma_f)}/r_{0.2(1\pm\sigma_f)})$ , where  $\sigma_f$  is the fractional error on the total flux. The total error on  $C$  should also include the uncertainty in the two isophotal radii values because of the pixel RMS noise. This error on the flux radii is not reported by SExtractor, and is cumbersome to compute for all sources. However we do not expect this additional uncertainty to greatly exceed our estimate based on  $C_{\pm}$ . In Figure 3 we plot the median  $C$  and median uncertainty in  $C$  for field sources in successive 1-mag bins (crosses with error bars). The uncertainty in  $C$  is  $\lesssim 0.05$  for sources with  $I \lesssim 24$ .

## 4. Discussion

### 4.1. Surface Brightness Profile Results for the *CXO* Counterparts

Examining the isophotal fitting results for the 22 resolved  $I < 24$  *CXO* counterparts (Fig. 1), we find that about half of the objects have a relatively flat color profile all the way into the nucleus, while a slightly smaller fraction display a nucleus that is at least half a magnitude bluer at its core than the average color across the rest of the galaxy. Three objects display nuclei that are redder by at least half a magnitude than their average global color.

We have searched for correlations between color gradient results and the X-ray properties of the galaxies. The three redder-centered objects appear to have somewhat harder X-ray spectra, while the flat-color objects are softer and in particular include all objects detected solely in the *CXO* soft band (0.5–2 keV). The bluer-centered objects have hardness ratios that are intermediate in value, covering the entire range from soft to hard. There is also some suggestion that the bluer-centered objects have a slightly higher  $L_X$  on average than the flat-color and redder-centered objects.

The correlation between higher  $L_X$  and blue central color gradient is expected since the bluer-centered objects are probably all type 1 AGN and are therefore detected at somewhat higher distances on average. This is confirmed by the optical spectroscopy that we have so far: all 3 of the 8 bluer-centered objects for which we have spectroscopic classifications (Szokoly et al. 2003, in prep.) are type 1’s; all 4 of the spectroscopic classifications available for the 16 flat-color and redder-centered objects suggest that they are type 2’s. Finally, the bluer-centered objects are found mostly in elliptical hosts (according to our morphological classifications), while the flat-centered objects are found in both spiral and elliptical hosts.

### 4.2. The Ratio of Obscured to Unobscured AGN at $z \sim 0.5$ –1

Most of the optically brighter *CXO* counterparts for which we estimated the nuclear point-source flux (3.2) also have measured redshifts (Szokoly et al., in prep.) which imply  $L_X \gtrsim 10^{42.5}$ . Such large X-ray luminosities are associated with AGN or intense starbursts — in either case the X-ray output of the host galaxy is dominated by the nuclear regions. Thus we can use our estimates of the unresolved nuclear flux in the CDFS counterparts to provide a much cleaner investigation of X-ray sources’  $F_X/F_{\text{opt}}$ . Figure 4 shows two plots of 2–10 keV  $F_X$  versus  $F_{\text{opt}}$  for the 1 Ms CDFS sources in our fields: the top panel shows  $F_{\text{opt,tot}}$  of the entire host (including nucleus), analogous to Figure 8 of Paper I for the

300 ksec CDFS sources; the bottom panel shows  $F_{\text{opt,nuc}}$  of the counterparts which are either unresolved (filled star symbols) or resolved but with finite unresolved nuclear flux (open star symbols). In the bottom panel, we also pair each  $F_{\text{opt,nuc}}$  with the corresponding  $F_{\text{opt,tot}}$  (dotted symbols) for comparison with the top panel. Here and throughout the rest of the discussion, we focus on the  $I$ -band data in preference to the  $V$ -band, since only the former samples rest-frame optical light ( $\gtrsim 4000\text{\AA}$ ) at the substantial redshifts ( $z \sim 0.5\text{--}1$ ) of even the brighter resolved *CXO* counterparts.

It is immediately obvious from Figure 4 that the scatter in  $F_X/F_{\text{opt}}$  is greatly reduced when considering only the optical flux originating from an unresolved nucleus — most have  $\log(F_X/F_{\text{opt,nuc}}) \sim 1.1 \pm 0.3$ . In particular, we see that the  $F_X/F_{\text{opt,nuc}}$  values for the resolved CDFS sources are now consistent with the narrow range of  $F_X/F_{\text{opt}}$  of the several *HST*-unresolved counterparts — all spectroscopically-confirmed type 1 AGN (Szokoly et al., in prep.). We may therefore infer that we are seeing type 1 AGN in these additional resolved hosts, bringing the total fraction of brighter CDFS counterparts with unobscured AGN to  $\sim 50\%$ .

Even these brighter optical CDFS counterparts are at substantial distances ( $z \sim 0.5\text{--}1$ ; Szokoly et al., in prep.), yet their type 1 fraction is comparable with recent measures of unbiased AGN samples at lower redshift (Wilkes et al. 2002). The hard-X-ray sensitivity of *CXO* can detect even highly-obscured AGN ( $N_H \sim 10^{24} \text{ cm}^{-2}$ ) of moderate luminosities ( $L_X \gtrsim 10^{42.5} \text{ erg s}^{-1}$ ) in the 1 Ms CDFS out to  $z \gtrsim 1$ , leading us to conclude that our current sample, albeit modest, does not support a steep redshift evolution in the type 2/type 1 ratio as favored by recent AGN synthesis models (e.g., Gilli et al. 2001).

### 4.3. Asymmetry of X-ray Hosts versus Field Galaxies

Having measured the asymmetry and concentration indices of all sources appearing in our three WFPC2 pointings (§3.3), we can make statistical comparisons of these morphological indicators between the *CXO*-detected and the *CXO*-undetected sources. Figure 5 shows the cumulative distribution of asymmetry index  $A$  for the 21 *CXO*-detected and *HST*-resolved sources with  $I < 23$  (heavy solid line) and for the remaining 267 galaxies with  $I < 23$  but undetected by *CXO*. The two distributions are statistically indistinguishable according to the Kolmogorov-Smirnov (K-S) test, which gives a 56% probability of the null hypothesis that they are drawn from the same underlying distribution.

Our finding that the brighter resolved CDFS sources, almost all at moderate redshifts  $z \sim 0.5\text{--}1$ , have a strikingly similar asymmetry distribution to the  $I < 23$  field may be

compared with earlier morphological studies of the *local* AGN population. For example, Corbin (2000) finds that the 45 galaxies in the Seyfert and LINER subsets of the BJC00 sample do not show significant asymmetry index differences compared with the 60 galaxies among the non-active subsets. *N*-body simulations of galaxy interactions (Walker, Mihos & Hernquist 1996) suggest that even minor mergers induce sufficient morphological disturbances to be detectable via the asymmetry index up to  $\sim 1$  Gyr after the onset of the merger. On this basis, Corbin (2000) concludes that minor mergers either have *no* role in the triggering of lower-luminosity AGN, or that the AGN manifests only in the late stages of the mergers — implying that the nuclei in his nearby sample have only been active within the last  $\sim 0.1$  Gyr.

Inasmuch as the hard X-ray sensitivity of the CDFS provides a near-complete census of both obscured and unobscured AGN at  $z \lesssim 1$  down to modest luminosities, similar to the BJC00 sample, the CDFS counterparts’ unexceptional asymmetries and paucity of obvious merger candidates ( $A > 0.35$ ; C. Conselice 2003, private comm.) now suggest that very recent merger history is not a good indicator of AGN activity over a substantial range of lookback time. If galaxy mergers are indeed a primary driver of AGN fueling, as has been commonly hypothesized (e.g. Gunn 1979, Dahari 1984, Roos 1985, Taniguchi 1999), then the epoch of AGN activity cannot closely coincide with that of merger-induced morphological disturbance —  $\lesssim 10^9$  yr.

#### 4.4. Companions to X-ray Hosts versus Field Galaxies

As a further check into the merger–AGN connection, we took a census of near neighbors to the CDFS counterparts. In Figure 6 we plot a histogram of the number of  $I < 23$  galaxies appearing within  $8''$  of the  $I < 23$  CDFS counterparts (heavier solid line). For comparison, we also plot the histogram of  $I < 23$  galaxies appearing within  $8''$  of the *CXO*-undetected  $I < 23$  population (lighter solid line). We adopt an angular separation threshold rather than a projected linear distance because we currently lack redshift information for most of the field galaxy control sample. However we note that  $8''$  corresponds to a narrow range of angular diameter distance,  $\approx 50$ – $65$  kpc, over a broad redshift range  $0.5 < z < 5$  in our adopted cosmology. This redshift range includes almost all the CDFS counterparts at  $I < 23$ , whose redshift survey is virtually complete (Szokoly et al., in prep.), and presumably the majority of the  $I < 23$  field galaxies. If the  $I < 23$  galaxies were not clustered, an  $8''$  radius would on average contain 1.1 such objects given their source density over the  $\approx 14.7$  arcmin<sup>2</sup> of our three WFPC2 fields. We show the corresponding Poisson distribution in Figure 6 (dotted line) for reference.

Compared with the X-ray-undetected  $I < 23$  population, the CDFS counterparts show an enhancement in the fraction with a single near neighbor and a corresponding deficit of isolated systems; the fraction with multiple companions is almost identical between the two populations. While it is obvious that the near-neighbor frequency histogram (Fig. 6) shows greater discrepancy between the X-ray host and field populations than the asymmetry parameter, nonetheless the  $\chi^2$  statistic between the two histograms gives only a modest rejection of the null hypothesis ( $\text{Prob}(\chi^2) = 0.019$ ) that the nearest-neighbor frequencies are consistent. Larger samples are clearly needed to establish the significance of a bias against isolated CDFS sources (see §5). As the current data do not support a significant enhancement in the fraction of CDFS sources with near neighbors, this reinforces our interpretation from the asymmetry analysis (§4.3) that there is no strong association between low- to moderate-luminosity AGN at moderate redshifts and recent/ongoing merger activity of the host galaxies. Similar conclusions at low redshift have emerged from recent studies of the AGN fractions among close pairs versus the field (Barton, Geller, & Kenyon 2000), and of the companion fractions of AGN versus non-AGN (Schmitt 2001).

#### 4.5. Central Concentration of X-ray Hosts versus Field Galaxies

Figure 7 shows the cumulative distribution of concentration index  $C$  for the 21 *CXO*-detected and *HST*-resolved sources with  $I < 23$  (heavier line) and for the remaining 267 galaxies with  $I < 23$  but undetected by *CXO* (lighter line). In marked contrast to the result for the asymmetry index, the two distributions of  $C$  are clearly distinct and have a low K-S probability of  $4.3 \times 10^{-6}$  for the null hypothesis.

Even though we have restricted this comparison to the *HST*-resolved CDFS counterparts, i.e. those whose optical flux is not dominated by the central engine, one may still worry that their concentration indices may be biased by the presence of optical flux from the AGN. Indeed we have found several of the CDFS host galaxies to be best-fit with a nuclear point source comprising  $\sim 1 - 10\%$  of the total flux (Fig. 4).

In theory, our two-dimensional modeling could be used to refine the  $C$  estimates by removing nuclear point-source bias. For example, one may consider computing  $C$  from a galaxy image *after* subtracting the best-fit nuclear point source. The model PSF does not precisely match the shape of the true PSF, however, and scaled PSF subtraction leaves relatively large-amplitude residuals in the host’s central pixels which hamper  $C$  estimation via SExtractor. Alternately, one may consider computing  $C$  from a model galaxy image constructed from the other, non-point-source, parameters in the two-dimensional fit. In practice this approach also fails, as our simulations indicate the two-dimensional fitting

robustly recovers the point-source flux but not the input bulge and disk shape parameters. Furthermore, a proper comparison with the field control sample in either case would require extending the two-dimensional modeling and “nuclear point-source correction” to the whole population, which is beyond the scope of the current study. Fortunately, our calculations below suggest that any enhancement of  $C$  from nuclear point-source flux is at most a small fraction of the observed  $C$  discrepancy (Fig. 7) between *CXO* hosts and field.

The effect of added point-source flux to a galaxy’s concentration index is not straightforward, since the near-Gaussian *HST* PSF is significantly less concentrated than an exponential or  $R^{1/4}$  profile. Small additions of nuclear flux will cause  $C$  to rise as  $r_{20}$  shrinks faster than  $r_{80}$ , but when the point-source becomes sufficiently dominant the concentration will peak and then collapse to the lower  $C$  of the PSF. We have attempted to quantify this effect by creating a suite of model galaxies based on a fiducial galaxy profile typical of our  $I < 23$  CDFS counterparts: a PSF-convolved,  $I = 22$  deVaucouleurs profile with  $R_e = 5$  pixels ( $0.25''$ ). We then steadily increase the flux fraction in the point-source nucleus, and measure  $C$  as a function of the point-source fraction.

The result is plotted in Figure 8, where we see that the peak increase of  $C$  is only  $\sim 0.1$ . Over the range corresponding to our measured point-source fractions, the deviation is  $< 0.05$ . This is only  $\approx 10\%$  of the discrepancy seen in Figure 7, from which we conclude that the AGN host concentration bias is truly related to differences in the host galaxy structure, and not to the possibility of nuclear point-source flux contribution.

Graham et al. (2001) have found a tight correlation between SBH mass and host galaxy concentration index exists among the nearby galaxy samples which previously established the close correlation between SBH mass and host bulge velocity dispersion (Ferrarese & Merritt 2000, Gebhardt et al. 2000). Although our initial analysis reveals little correlation between  $L_X$  (as a proxy for SBH mass) and  $C$  for the  $I < 23$  CDFS host galaxies, it is likely that our sample — almost all with hard X-ray luminosities indicative of AGN ( $L_X > 10^{42.5}$  ergs  $s^{-1}$ ) — harbor SBHs at the high end of the SBH mass function relative to the X-ray undetected galaxies in our fields. Our WFPC2 findings therefore suggest, for the first time, that the close linkage between SBH mass and host galaxy properties extends to the substantial look-back times ( $z \sim 0.5 - 1$ ) typical of the  $I < 23$  CDFS X-ray sources.

## 5. Summary

The deep fields observed with the *Chandra X-ray Observatory* have produced the first large uniform catalogs of X-ray sources down to modest AGN luminosities ( $L_X \sim$

$10^{42-42.5}$  erg  $s^{-1}$ ) at substantial redshift. Given the good hard-X-ray sensitivity of the CDFS observations, this catalog is expected to provide a near-complete census of both obscured and unobscured AGN at  $z \lesssim 1$ , whose redshifts appear to be concentrated in the range  $z \sim 0.5 - 1$  (Rosati et al. 2002; Szokoly et al., in prep.). We have presented this first quantitative morphological study of many optical counterparts of these distant AGN based on our deep *HST* observations of three WFPC2 fields in the CDFS.

We have compared the asymmetry indices of  $I < 23$  AGN hosts with the much larger population of similarly bright X-ray-undetected field galaxies. We find a very good agreement between the asymmetry distributions of the two populations (Fig. 5). Furthermore, the *CXO* counterparts show only a modest difference from the field population in the frequency of nearby companions (Fig. 6). These findings are similar to studies of comparable low-redshift populations, and now suggest that recent merger history is not a good indicator of AGN activity over a substantial range of lookback time.

Our PSF-convolved two-dimensional profile fitting of the *HST*-resolved *CXO* counterparts shows that over a third have significant nuclear point-source emission. The  $F_X/F_{\text{opt}}$  of these unresolved nuclear sources is consistent with the narrow  $F_X/F_{\text{opt}}$  range of the several *HST*-unresolved counterparts (Fig. 7). We therefore infer that the total fraction of  $I < 24$  CDFS counterparts harboring type 1 AGN is  $\sim 50\%$ , consistent with recent findings for unbiased AGN samples at lower redshift (Wilkes et al. 2002). If the large type 1 fraction inferred from our modest sample were representative of the overall  $z \sim 0.5-1$  AGN population, this would be problematic for recent AGN synthesis models (e.g. Gilli et al. 2001) which favor a sharp rise in the type 2/type 1 ratio out to  $z \sim 1$ .

Our comparison of the concentration indices of *CXO* counterparts with the field reveals a clear bias toward higher  $C$  among the *CXO* host galaxies (Fig. 7). This  $\sim 5\sigma$  result does not appear to be an artifact of heightened optical flux from the CDFS hosts' nuclei, and may represent the first evidence that the locally-observed correlation between SBH mass and host-galaxy properties, including concentration index, is already in place by  $z \sim 1$ .

To press upon these results regarding the merger–AGN connection and SBH–host-galaxy connection at moderate- to high-redshift, we are undertaking extensive *HST*/Advanced Camera for Surveys (ACS) multicolor imaging of the two *Chandra* Deepest Fields as part of the Great Observatories Origins Deep Survey (GOODS, Dickinson & Giavalisco 2003). The GOODS data will both increase by  $\gtrsim 10$  times the available number of *HST*-imaged AGN hosts and comparison field galaxies in *CXO*  $\gtrsim 1$  Ms fields and also will provide extensive spectroscopic and photometric redshift coverage to complement the ACS morphologies. With  $> 400$  *HST* counterparts of  $\gtrsim 1$  Ms *CXO* sources, we will solidly verify the morphological and environmental conclusions we have drawn from the 37 CDFS host galaxies in the present

work. Furthermore, the large sample in combination with multicolor imaging and redshift information will allow us to track the *evolution* of AGN versus non-AGN environment and rest-frame *B* morphology out to  $z \sim 1.3$  (Grogin et al. 2003).

We thank C. Conselice for insightful discussions and for graciously providing his asymmetry-index code for our use. We thank R. Gilli and the anonymous referee for comments which strengthened the manuscript. We gratefully acknowledge the award of *HST* Director’s Discretionary time in support of this project. We also acknowledge support for this work which was provided by NASA through GO grants GO-08809.01-A and GO-07267.01-A from the Space Telescope Science Institute, which is operated by AURA, Inc., under NASA Contract NAS 5-26555.

## REFERENCES

- Abraham, R. G., Merrifield, M. R., Ellis, R. S., Tanvir, N. R., & Brinchmann, J. 1999, MNRAS, 308, 569
- Barton, E. J., Geller, M. J., & Kenyon, S. J. 2000, ApJ, 530, 600
- Bershady, M. A., & Jangren, A., & Conselice, C. J. 2000, AJ, 119, 2645 (BJC00)
- Bertin, E. & Arnouts, S. 1996, A&AS, 117, 393
- Brandt, W. N., Alexander, D. M., Hornschemeier, A. E., Garmire, G. P., Schneider, D. P., Barger, A. J., Bauer, F. E., Broos, P. S., Cowie, L. L., Townsley, L. K., Burrows, D. N., Chartas, G., Feigelson, E. D., Griffiths, R. E., Nousek, J. A., & Sargent, W. L. W. 2001, AJ, 122, 2810
- Casertano, S., de Mello, D., Dickinson, M., Ferguson, H. C., Fruchter, A. S., Gonzalez-Lopezlira, R. A., Heyer, I., Hook, R. N., Levay, Z., Lucas, R. A., Mack, J., Makidon, R. B., Mutchler, M., Smith, T. E., Stiavelli, M., Wiggs, M. S., Williams, R. E. 2000, AJ, 120, 2747
- Conselice, C. J., Bershady, M. A., & Jangren, A. 2000, ApJ, 529, 886
- Corbin, M. R. 2000, ApJ, 536, L73
- Cowie, L. L., Barger, A. J., Bautz, M. W., Brandt, W. N., & Garmire, G. P. 2003, ApJ, 584, L57
- Dahari, O. 1984, AJ, 89, 966
- Dickinson, M. E., Giavalisco, M. 2003, in Proc. ESO/USM Workshop, The Mass of Galaxies at Low and High Redshift, ed. R. Bender & A. Renzini (Berlin: Springer), 324

- Ferrarese, L. & Merritt, D. 2000, *ApJ*, 539, 9
- Fruchter, A. S. & Hook, R. N. 2001, *PASP*, 114, 144
- Gebhardt, K., Kormendy, J., Ho, L. C., Bender, R., Bower, G., Dressler, A., Faber, S. M., Filippenko, A. V., Green, R., Grillmair, C., Lauer, T. R., Magorrian, J., Pinkney, J., Richstone, D., & Tremaine, S. 2000, *ApJ*, 539, 13
- Giacconi, R., Zirm, A., Wang, J. X., Rosati, P., Nonino, M., Tozzi, P., Gilli, R., Mainieri, V., Hasinger, G., Kewley, L., Bergeron, J., Borgani, S., Gilmozzi, R., Grogin, N., Koekemoer, A., Schreier, E., Zheng, W. & Norman, C. 2002, *ApJ*, 139, 369
- Gilli, R., Salvati, M., & Hasinger, G. 2001, *A&A*, 366, 407
- Graham, A. W., Erwin, P., Caon, N., Trujillo, I. 2001, *ApJ*, 563, L11
- Grogin, N. A., Conselice, C. J., Chatzichristou, E., Alexander, D. M., Bauer, F. E., Hornschemeier, A. E., Jogee, S., Koekemoer, A. M., Laidler, V. G., Lucas, R. A., Paolillo, M., Ravindranath, S., Schreier, E. J., Simmons, B. D., & Urry, C. M. 2003, *ApJL*, submitted
- Gunn, J. E. 1979, in *Active Galactic Nuclei*, ed. C. Hazard & S. Mitton (Cambridge: Cambridge Univ. Press), 213
- Hasinger, G., Lehmann, I., Giacconi, R., Schmidt, M., Trümper, J., & Zamorani, G. 1999, in *Highlights in X-Ray Astronomy*, ed. B. Aschenbach & M. J. Freyberg (MPE Rep. 272; Garching: MPE), 199
- Hornschemeier, A. E., Brandt, W. N., Garmire, G. P., Schneider, D. P., Barger, A. J., Broos, P. S., Cowie, L. L., Townsley, L. K., Bautz, M. W., Burrows, D. N., Chartas, G., Feigelson, E. D., Griffiths, R. E., Lumb, D., Nousek, J. A., Ramsey, L. W., & Sargent, W. L. W. 2001, *ApJ*, 554, 742
- Koekemoer, A. M., Grogin, N. A., Schreier, E. J., Giacconi, R., Gilli, R., Kewley, L., Norman, C., Zirm, A., Bergeron, J., Rosati, P., Hasinger, G., Tozzi, P., & Marconi, A. 2002, *ApJ*, 567, 657 (Paper II)
- Krist, J. E. & Hook, R. 2001, *The Tiny Tim User's Guide*, Version 6.0 (Baltimore: STScI)
- Lilly, S., Schade, D., Ellis, R., Le Fevre, O., Brinchmann, J., Tresse, L., Abraham, R., Hammer, F., Crampton, D., Colless, M., Glazebrook, K., Mallen-Ornelas, G., & Broadhurst, T. 1998, *ApJ*, 500, 75
- Magorrian, J., Tremaine, S., Richstone, D., Bender, R., Bower, G., Dressler, A., Faber, S. M., Gebhardt, K., Green, R., Grillmair, C., Kormendy, J., & Lauer, T. 1998, *AJ*, 115, 2285
- Miyaji, T., Hasinger, G., & Schmidt, M. 2000, *A&A*, 353, 25

- Mushotzky, R., Cowie, L. L., Barger, A. J., & Arnaud, K. A. 2000, *Nature*, 404, 459
- Press, W. H., Flannery, B. P., Teukolsky, S. A., & Vetterling, W. T. 1992, *Numerical Recipes in C* (2d ed; New York: Cambridge Univ. Press)
- Roos, N. 1985, *ApJ*, 294, 479
- Rosati, P., Tozzi, R., Giacconi, R., Gilli, R., Hasinger, G., Kewley, L., Mainieri, V., Nonino, M., Norman, C., Szokoly, G., Wang, J. X., Zirm, A., Bergeron, J., Borgani, S., Gilmozzi, R., Grogin, N., Koekemoer, A., Schreier, E., & Zheng, W. 2002, *ApJ*, 566, 667
- Schreier, E. J., Koekemoer, A. M., Grogin, N. A., Giacconi, R., Gilli, R., Kewley, L., Norman, C., Hasinger, G., Rosati, P., Marconi, A., Salvati, M., & Tozzi, P. 2001, *ApJ*, 560, 127 (Paper I)
- Schmitt, H. R. 2001, *AJ*, 122, 2243
- Taniguchi, Y. 1999, *ApJ*, 524, 65
- Tozzi, P., Rosati, P., Nonino, M., Bergeron, J., Borgani, S., Gilli, R., Gilmozzi, R., Hasinger, G., Grogin, N., Kewley, L., Koekemoer, A., Norman, C., Schreier, E., Shaver, P., Szokoly, G., Wang, J. X., Zheng, W., Zirm, A. & Giacconi, R. 2001, *ApJ*, 562, 42
- Urry, C. M. & Padovani, P. 1995, *PASP*, 107, 803
- Walker, I. R., Mihos, J. C., & Hernquist L. 1996, *ApJ*, 460, 121
- Wilkes, B. J., Schmidt, G. D., Cutri, R. M., Ghosh, H., Hines, D. C., Nelson, B., & Smith, P. S. 2002, *ApJ*, 564, L65

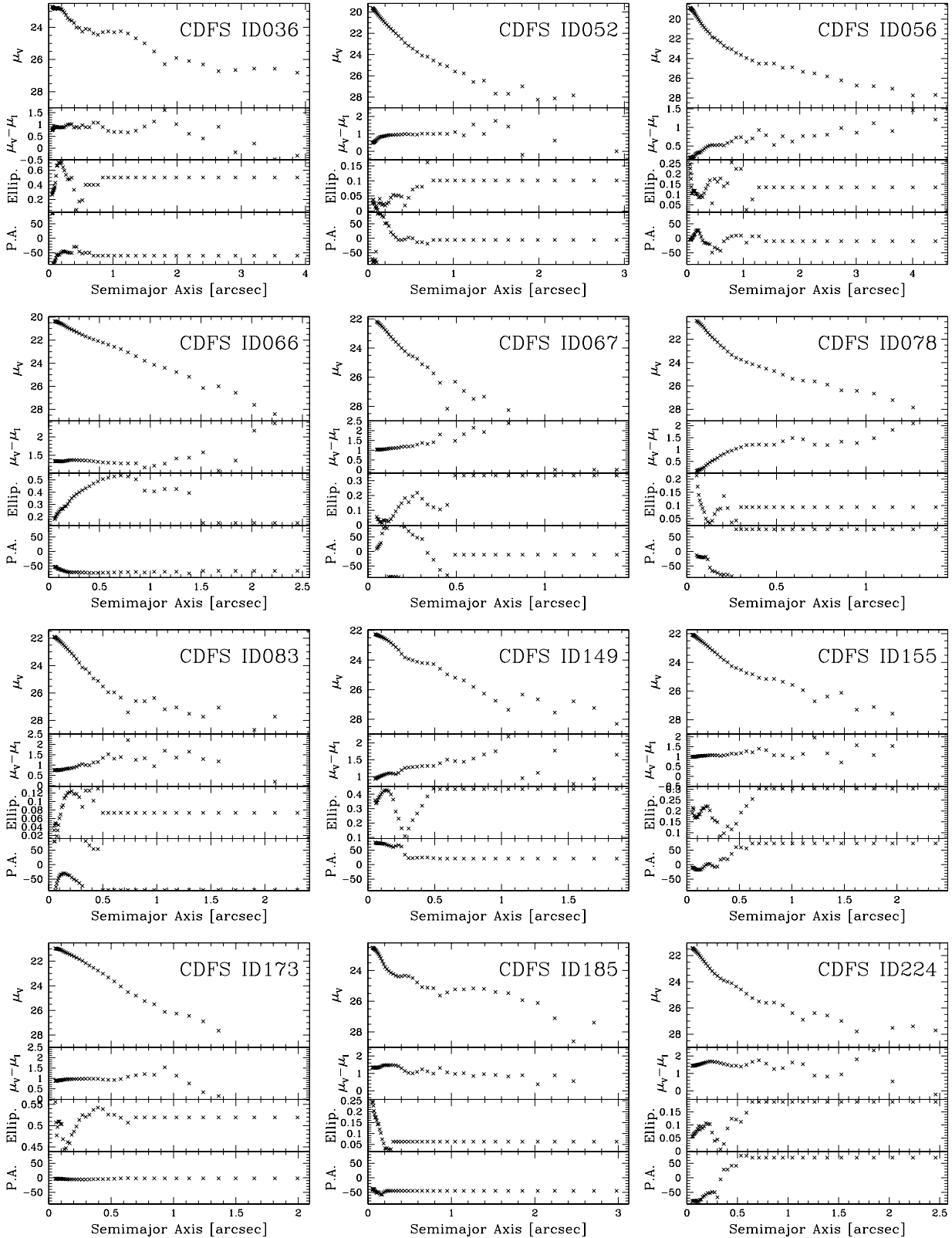


Fig. 1.— Isophotal surface photometry of *HST*-resolved  $I < 24$  counterparts to CDFS sources.

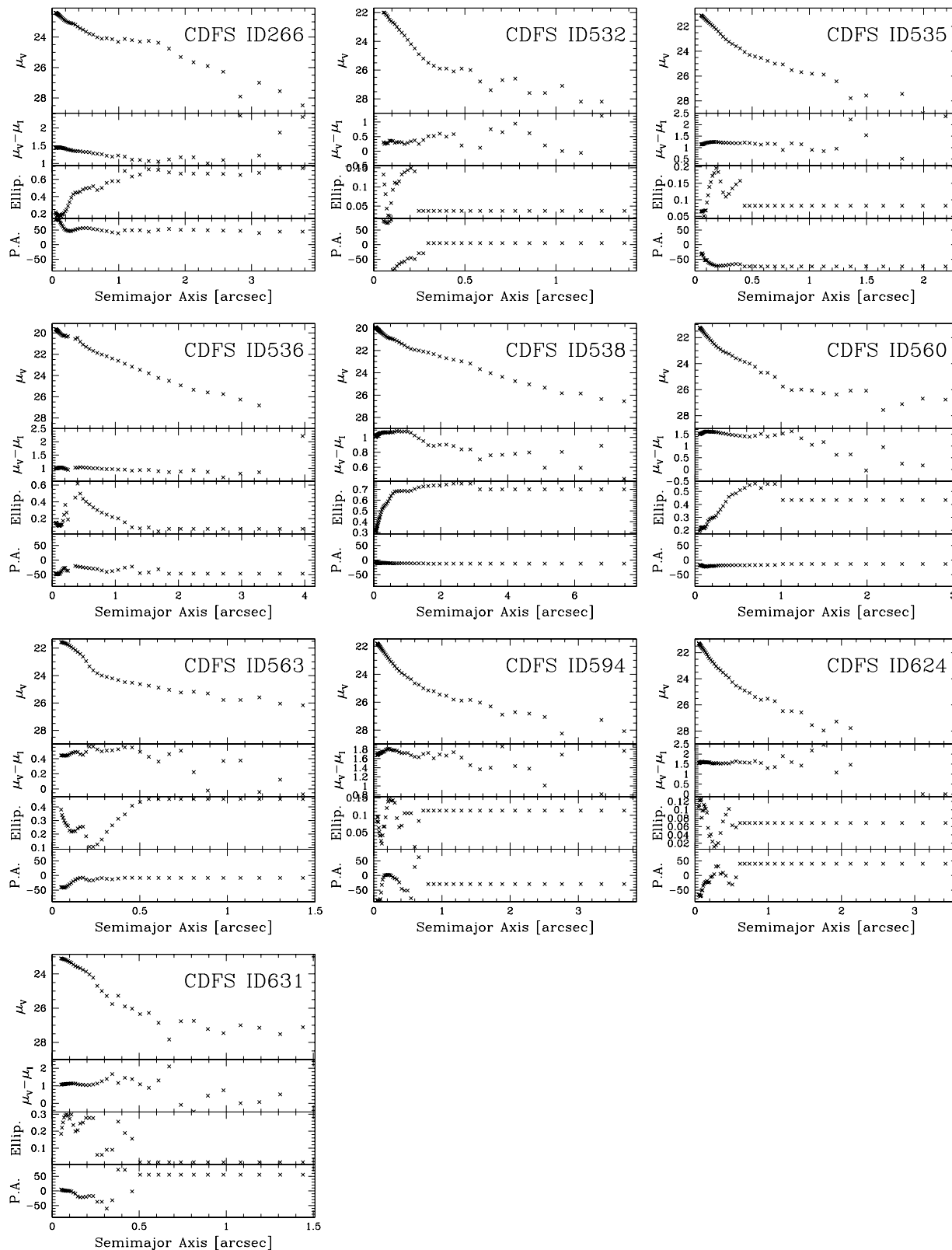


Fig. 1.— Cont'd.

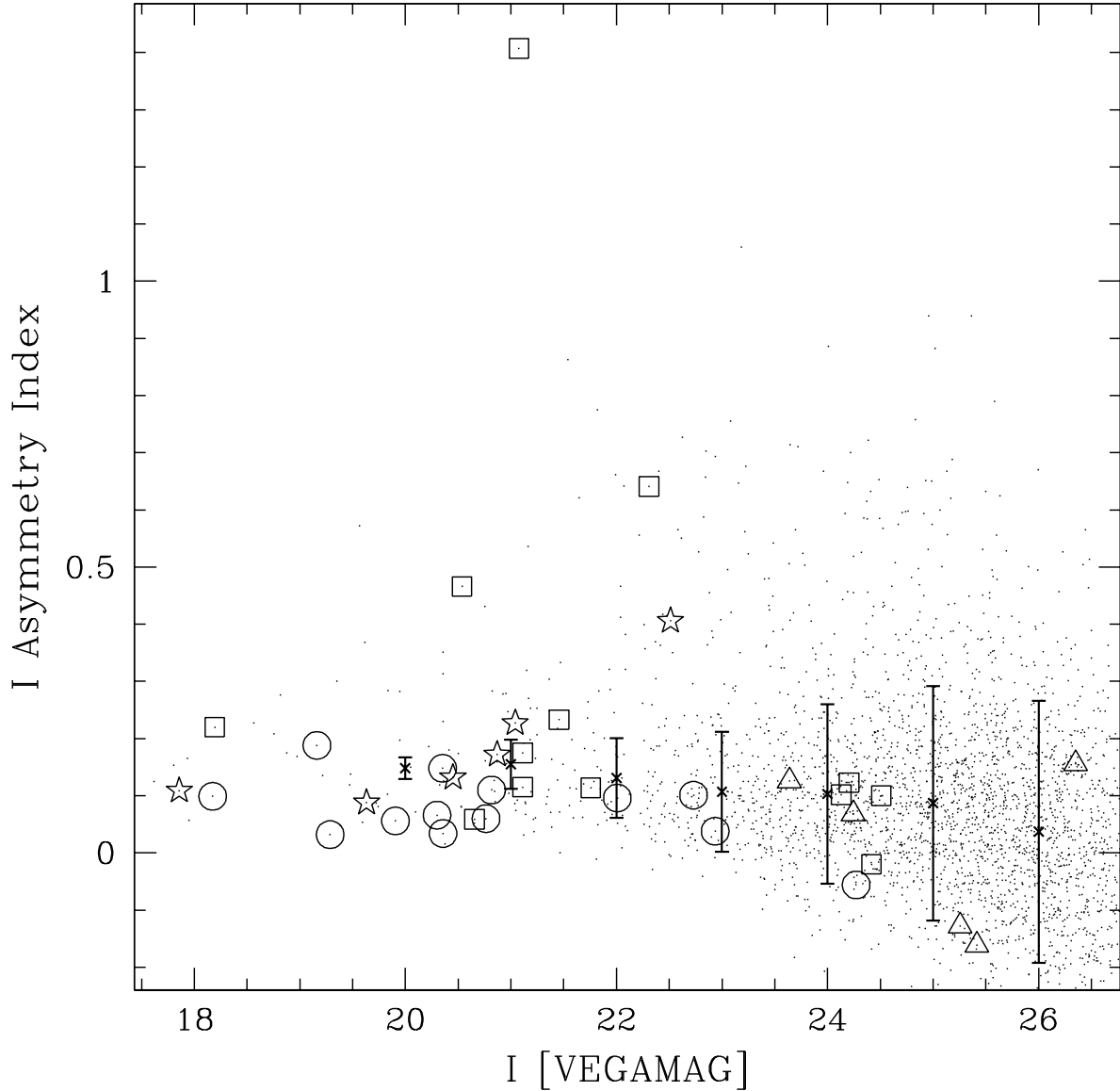


Fig. 2.— Asymmetry index,  $A$ , of the  $I$  surface brightness distributions for all detected sources in our three WFPC2 pointings (small dots) plotted as a function of total  $I$  magnitude. The sources detected by the 1 Ms *CXO* observation are flagged by large symbols keyed to morphological type: E/S0 (circles); S/Irr (squares); unresolved (stars); and indeterminate (triangles). The crosses and their associated error bars respectively denote the median  $A$  and the median uncertainty in  $A$  for field sources within successive 1.0-mag bins.

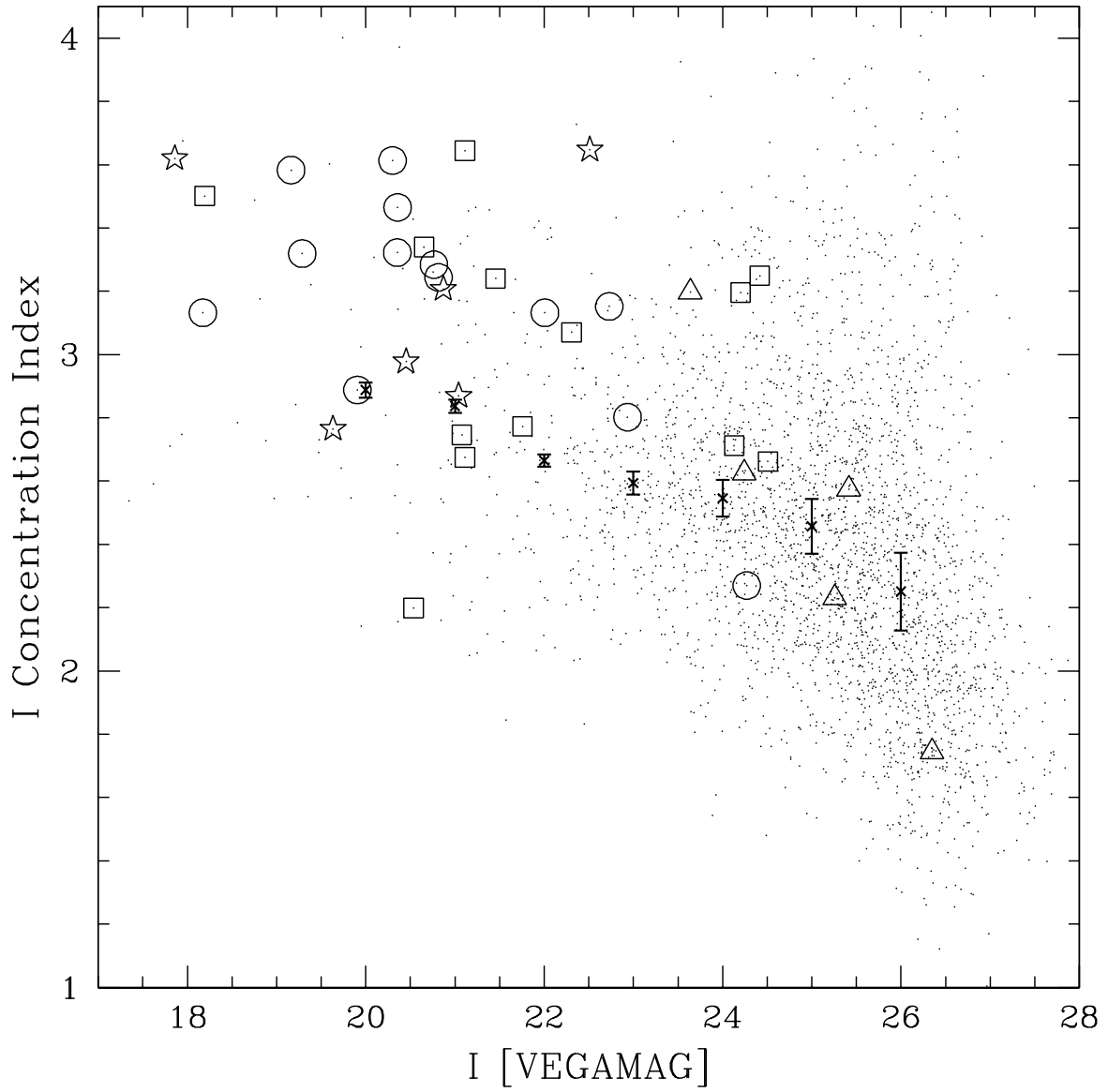


Fig. 3.— Same as Fig. 2, but for concentration index  $C$

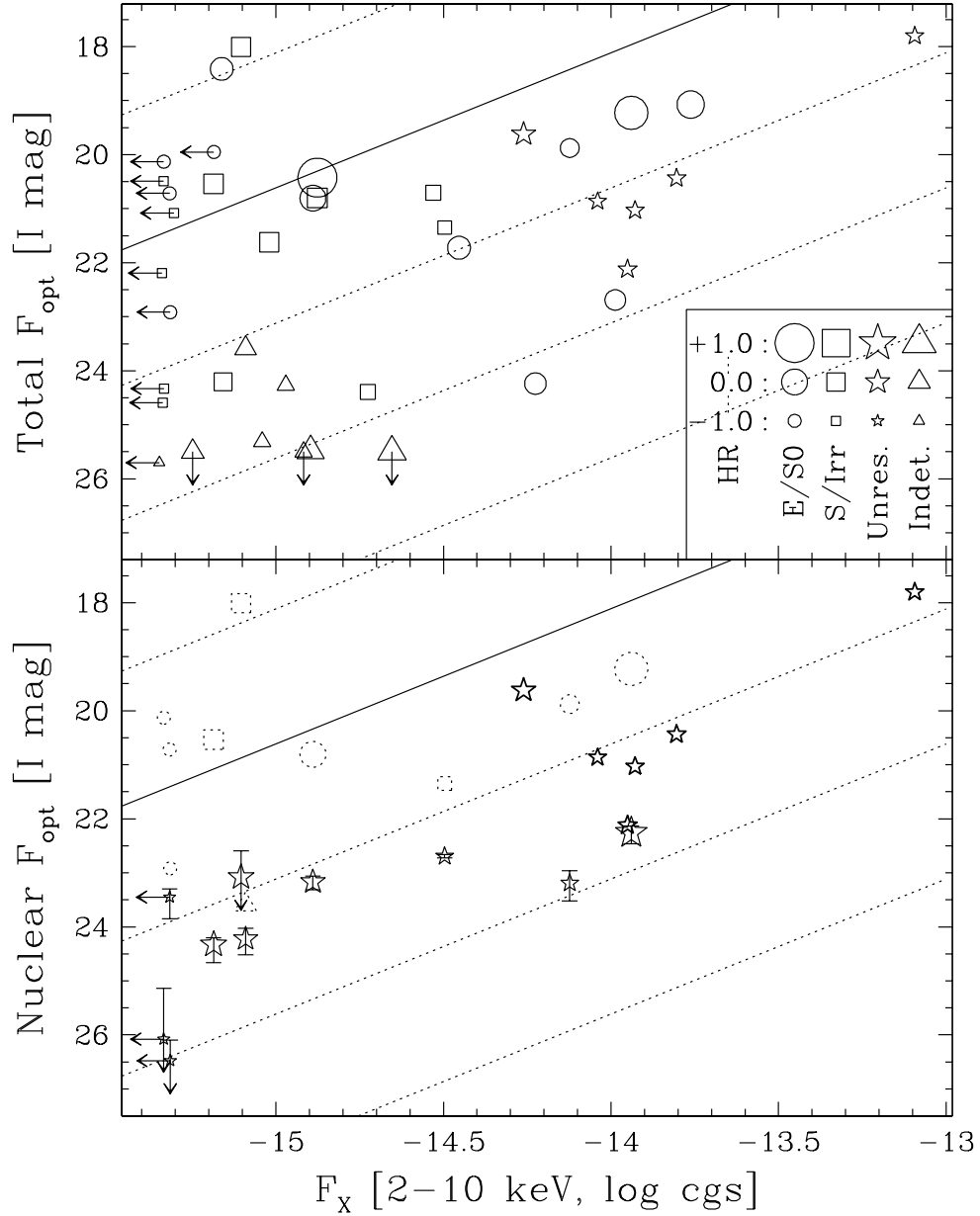


Fig. 4.—  $F_X$  versus  $F_{\text{opt}}$  plots showing: a) integrated optical flux for all *CXO* sources. X-ray hardness of the source is indicated by symbol size, and host optical morphology is indicated by symbol shape, as noted in the legend; b) optical unresolved nuclear flux for the subset of  $I < 24$  counterparts best-fit with a finite nuclear point-source. Resolved hosts are now shown as open stars, below their corresponding dotted symbol denoting total  $F_{\text{opt}}$  and host morphology. The unresolved hosts are now plotted as filled stars. Diagonal lines are 1-dex intervals of  $F_X/F_{\text{opt}}$ , with the solid line denoting  $F_X/F_{\text{opt}} = 1$

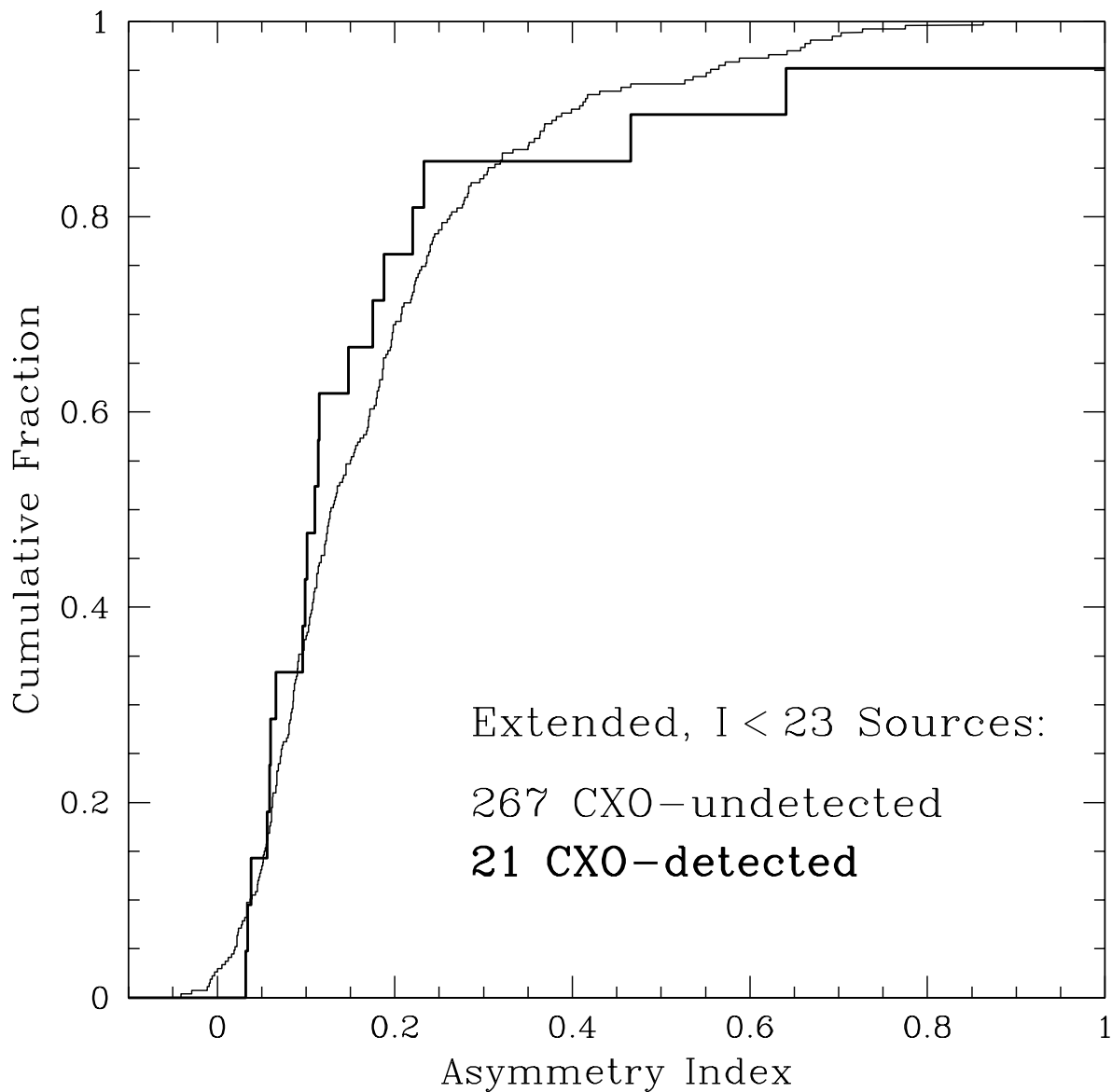


Fig. 5.— Cumulative distribution functions of asymmetry index for bright resolved sources ( $I < 23$ ;  $\eta_V < 0.5$ ) in our three WFPC2 pointings in the Chandra Deep Field South. The heavier line corresponds to those sources also detected in the 1 Ms *CXO* exposure; the lighter line corresponds to the *CXO*-undetected sources.

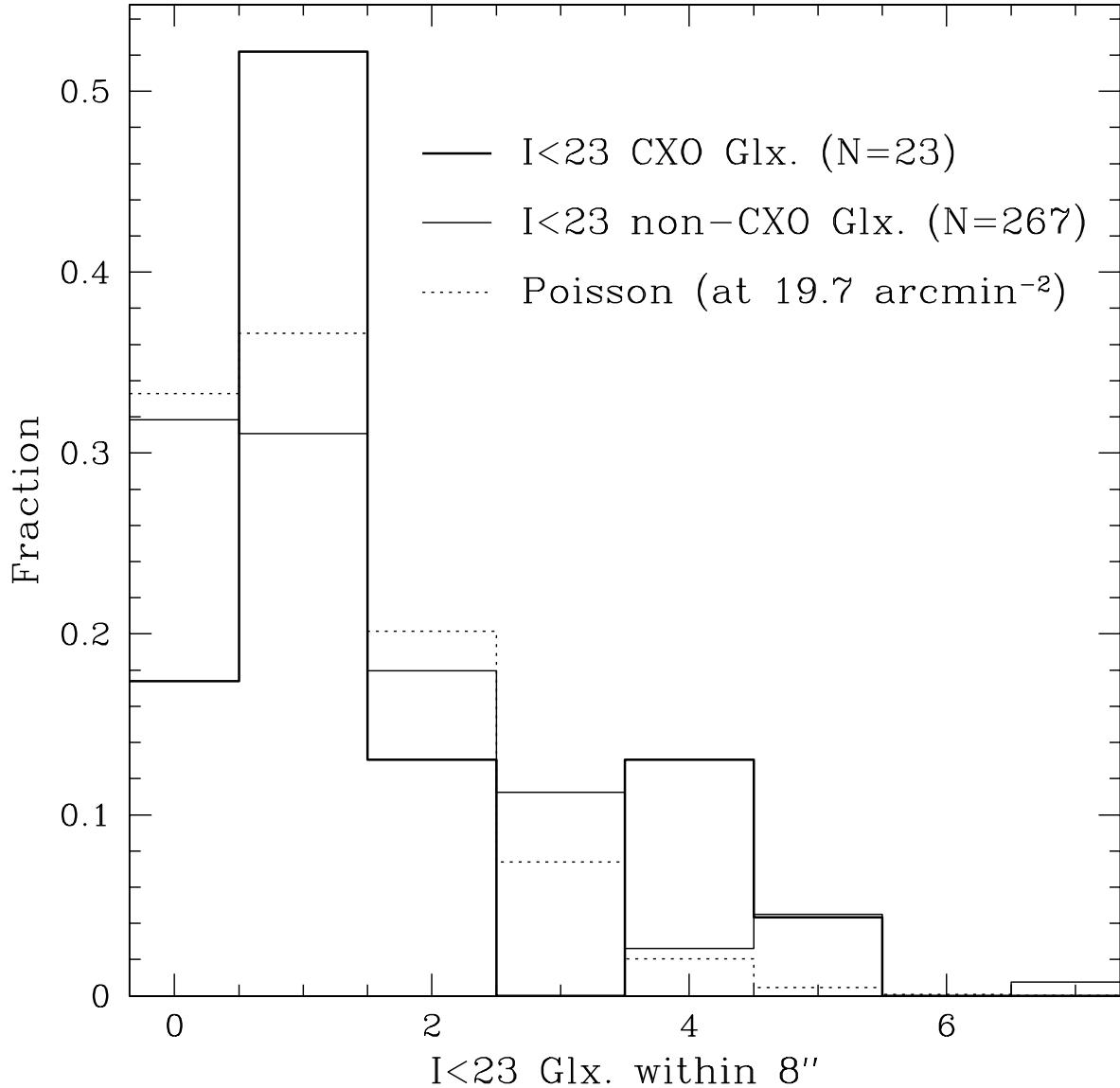


Fig. 6.— Histogram of the number of nearby ( $< 8''$ )  $I < 23$  galaxies appearing around the 21 resolved CDFS counterparts with  $I < 23$  (heavy solid line) and around the 267 non-CXO-detected galaxies in our catalog with  $I < 23$  (light solid line). These two histograms are normalized by the sample sizes. For comparison we also show the expected histogram if the  $I < 23$  galaxies were distributed at random given their observed number density (dotted line).

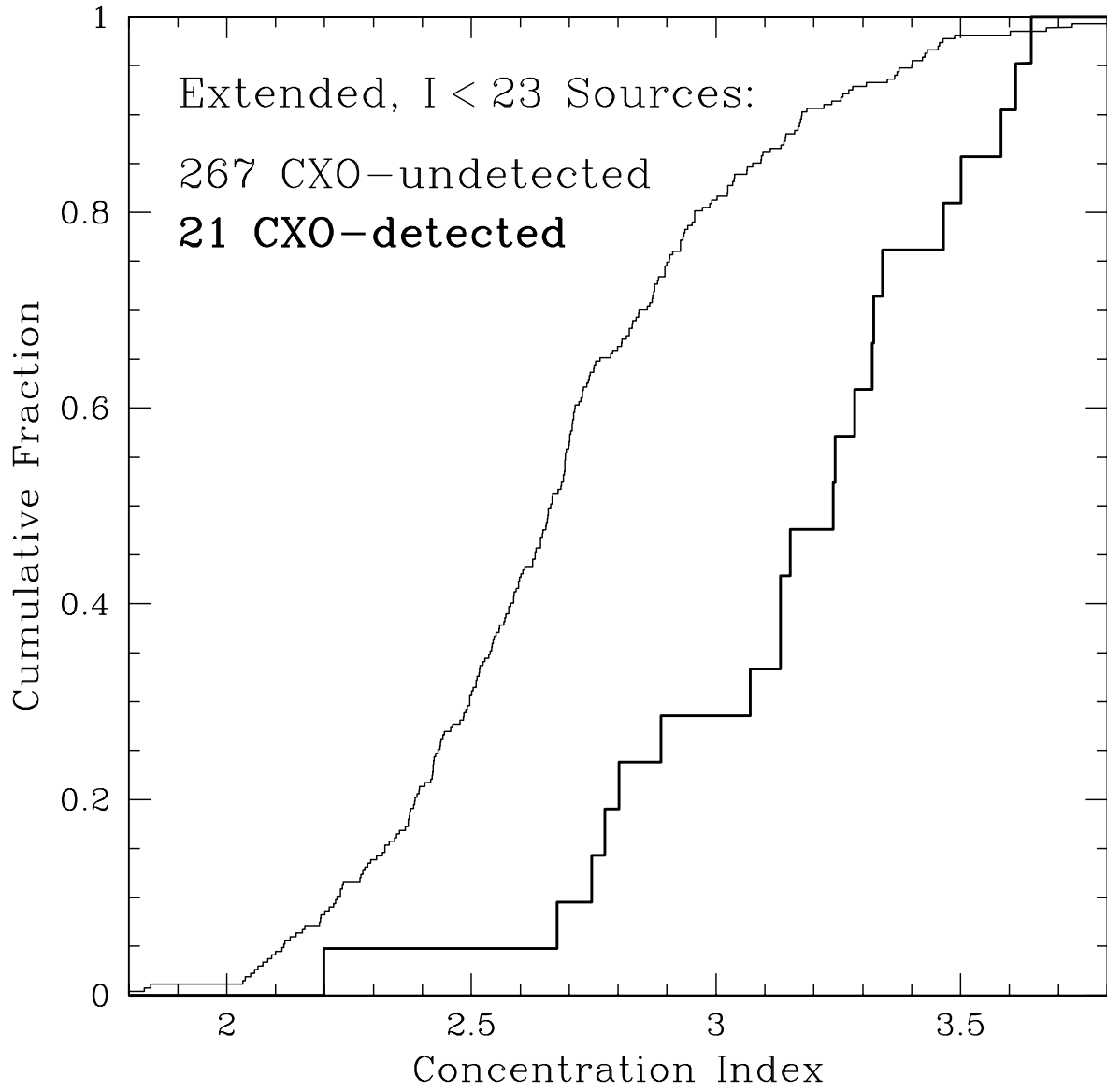


Fig. 7.— Same as Fig. 5, but for concentration index  $C$ .

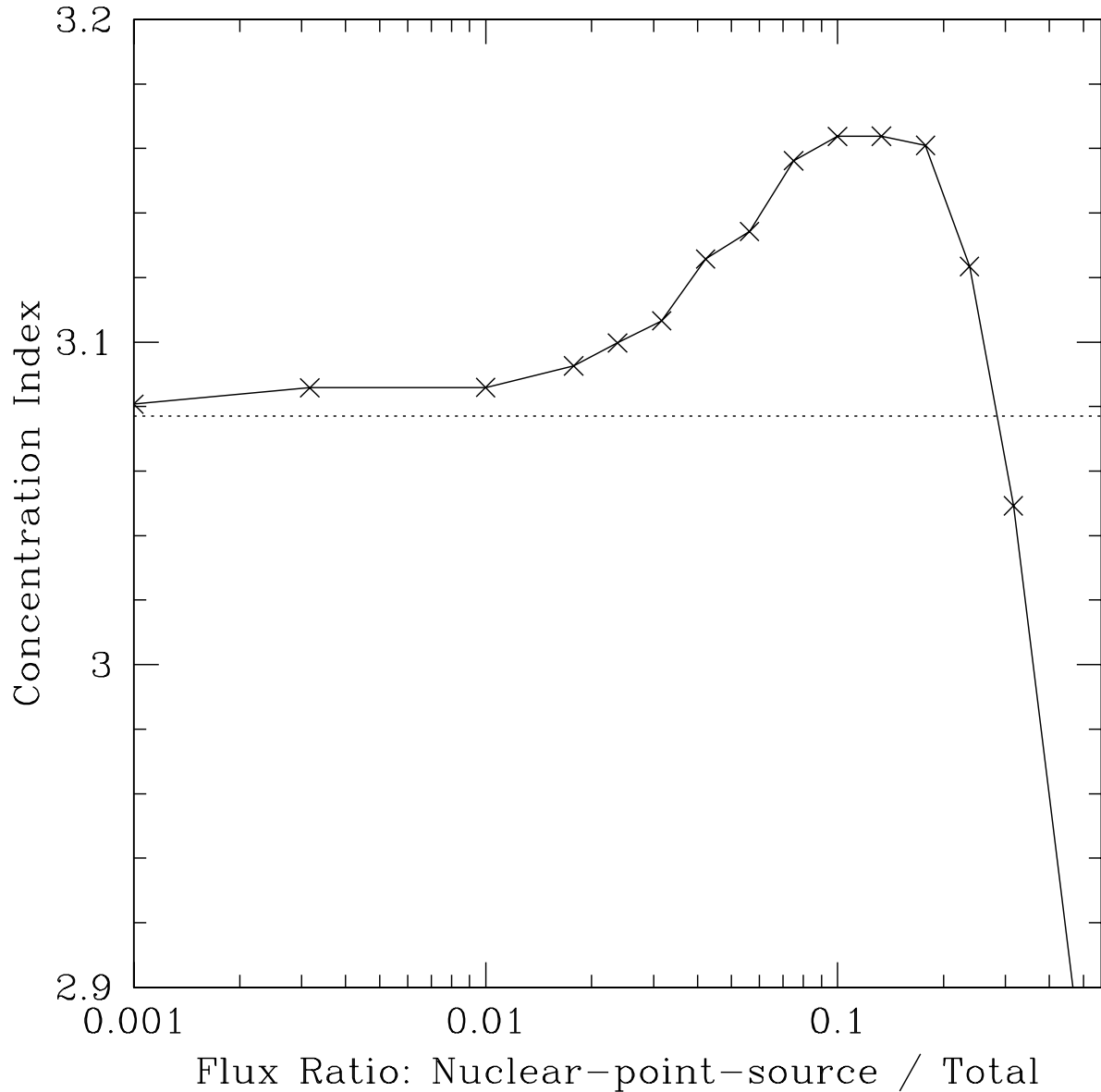


Fig. 8.— Simulation of the concentration index ( $C$ ) variation as a function of nuclear point-source flux fraction. The dotted line indicates  $C$  for the fiducial galaxy alone: an  $I = 22$  PSF-convolved deVaucouleurs profile with  $R_e = 5$  pixels ( $0''.25$ ). The comparatively low  $C$  of the PSF causes the turnover in the curve at large nuclear point-source flux fractions. The amplitude of the  $C$  increase remains small relative to the bias observed in Figure 7.

Table 1. WFC2 Source Catalog: Coordinates, Magnitudes, and Shape Parameters

$\alpha_{J2000}$ (deg)	$\delta_{J2000}$ (deg)	F606W (mag)	F814W (mag)	$r_{0.5,I}$ (arcsec)	$\eta_V$	$\eta_I$	$A_I$	$C_V$	$C_I$
53.007162	-27.769990	27.53	> 26.5	0.16	0.02	0.63	0.06	1.89	1.81
53.007943	-27.771112	26.43	25.16	0.24	0.00	0.00	0.03	2.47	2.82
53.008016	-27.770895	27.34	26.07	0.20	0.80	0.01	-0.01	3.34	2.88
53.008110	-27.771046	27.01	25.96	0.16	0.01	0.05	0.02	2.13	2.43
53.008349	-27.769775	24.52	22.73	0.29	0.02	0.02	0.30	2.28	2.63
53.008414	-27.771456	27.24	> 26.5	0.09	0.01	0.63	0.08	2.56	1.83
53.008675	-27.771753	26.00	25.35	0.11	0.00	0.00	0.27	2.60	2.20
53.009305	-27.767180	23.18	21.12	0.56	0.00	0.00	0.19	2.25	2.39
53.009428	-27.770188	27.34	> 26.5	0.07	0.53	0.56	-0.25	2.04	1.74
53.009442	-27.763427	24.83	23.08	0.38	0.00	0.02	0.76	2.43	2.13
53.009653	-27.767549	26.48	25.89	0.13	0.00	0.00	-0.11	3.02	2.76
53.009702	-27.765063	26.01	24.66	0.16	0.02	0.01	-0.05	3.16	2.89
53.009772	-27.766885	27.15	25.55	0.12	0.00	0.00	-0.21	2.89	2.16
53.009885	-27.770993	23.37	21.91	0.38	0.00	0.00	0.06	2.46	2.60
53.009959	-27.772112	26.23	25.24	0.14	0.00	0.00	-0.09	2.24	2.09
53.010116	-27.764251	> 27.8	26.05	0.10	0.06	0.01	-0.10	1.67	2.29
53.010253	-27.765836	26.04	24.24	0.37	0.00	0.00	0.07	3.85	3.02
53.010534	-27.766503	26.10	25.84	0.14	0.00	0.00	0.15	2.12	1.86
53.010582	-27.771649	24.37	22.94	0.38	0.00	0.00	0.21	2.04	2.42
53.010584	-27.767012	24.71	22.73	0.18	0.02	0.04	0.10	3.12	3.15
53.010590	-27.768191	24.21	23.29	0.38	0.00	0.00	0.09	2.33	2.23
53.010664	-27.766375	27.41	> 26.5	0.10	0.02	0.00	-0.18	1.61	1.86
53.010679	-27.769254	27.25	25.65	0.15	0.00	0.00	-0.09	2.09	2.86
53.010681	-27.761041	> 27.8	25.99	0.12	0.01	0.00	0.17	1.62	1.79
53.010846	-27.760243	23.13	21.56	0.18	0.03	0.03	0.11	2.69	2.82
53.010918	-27.764613	27.12	25.53	0.12	0.03	0.00	0.19	2.07	2.77
53.011001	-27.765044	27.28	25.93	0.19	0.01	0.00	-0.14	2.35	1.97
53.011020	-27.766578	26.36	24.87	0.20	0.00	0.00	0.11	3.73	2.55
53.011088	-27.769922	27.15	25.91	0.17	0.00	0.01	-0.30	3.68	2.87
53.011158	-27.766516	27.71	25.53	0.14	0.00	0.00	0.35	3.14	1.91
53.011179	-27.762714	27.19	> 26.5	0.08	0.04	0.02	0.23	1.92	2.48
53.011219	-27.772550	> 27.8	25.54	0.21	0.05	0.00	0.09	2.48	1.91
53.011291	-27.760761	25.41	23.88	0.56	0.00	0.00	0.15	2.69	2.08
53.011320	-27.760891	26.56	25.36	0.44	0.00	0.00	0.14	2.56	3.10
53.011347	-27.766480	> 27.8	> 26.5	0.10	0.01	0.02	0.28	1.86	2.25
53.011536	-27.764139	26.01	24.25	0.16	0.00	0.01	0.01	2.36	2.44
53.011569	-27.772637	24.62	23.56	0.25	0.00	0.00	-0.03	2.42	2.56
53.011587	-27.758720	27.52	26.39	0.15	0.00	0.01	-0.18	2.22	1.78
53.011632	-27.770297	26.61	25.32	0.21	0.00	0.00	0.05	3.27	2.63
53.011753	-27.770756	26.00	24.80	0.38	0.00	0.00	0.01	3.24	2.21
53.011806	-27.769385	26.97	26.31	0.10	0.01	0.00	0.19	2.04	1.86
53.011876	-27.767014	26.96	> 26.5	0.20	0.01	0.48	-0.06	1.98	1.17

Note. — Table 1 is available in its entirety by request from the authors, and will be published in the electronic edition of the *Astrophysical Journal*. A portion is shown here for guidance regarding its form and content.

Table 2. WFPC2 CDFS Counterparts: X-ray and Optical Properties

XID	IAU Designation	$\log F_{2-10\text{keV}}^{\text{a}}$ (cgs)	$H.R.^{\text{b}}$	F606W (mag)	F814W (mag)	$r_{0.5,I}$ ( $''$ )	$\eta_V$	$\eta_I$	$(f_{\text{nuc}}/f_{\text{tot}})_V^{\text{c}}$	$(f_{\text{nuc}}/f_{\text{tot}})_I^{\text{c}}$	$A_I$	$C_I$	Comments
36	J033233.1–274548	−14.53	−0.36	22.95	21.08	0.71	0.00	0.00	$0 < 0.0086$	$0 < 0.033$	$1.407 \pm 0.012$	$2.75 \pm 0.01$	In compact group
38	J033230.3–274505	−14.04	−0.56	22.18	20.87	0.16	0.69	0.03	$\sim 1^{\text{d}}$	$\sim 1^{\text{d}}$	$0.172 \pm 0.005$	$3.21 \pm 0.04$	
39	J033230.1–274530	−13.80	−0.47	21.34	20.45	0.14	0.87	0.15	$\sim 1^{\text{d}}$	$\sim 1^{\text{d}}$	$0.132 \pm 0.003$	$2.98 \pm 0.04$	
52	J033217.2–274304	−14.12	−0.54	21.57	19.91	0.25	0.03	0.03	$0.10 < 0.22$	$0.049^{+0.012}_{-0.012}$	$0.056 \pm 0.005$	$2.89 \pm 0.03$	
56	J033213.3–274241	−13.76	+0.11	20.83	19.16	0.35	0.03	0.03	$0.0096 < 0.066$	$0 < 0.011$	$0.188 \pm 0.004$	$3.58 \pm 0.03$	
58	J033211.8–274629	−14.73	−0.34	25.95	24.42	0.19	0.00	0.02	...	...	$-0.020 \pm 0.162$	$3.25 \pm 0.18$	
60	J033211.0–274415	−13.93	−0.48	22.39	21.04	0.13	0.54	0.41	$\sim 1^{\text{d}}$	$\sim 1^{\text{d}}$	$0.227 \pm 0.004$	$2.87 \pm 0.04$	
61	J033210.6–274309	−13.95	−0.44	25.09	22.51	0.20	0.83	0.73	$\sim 1^{\text{d}}$	$\sim 1^{\text{d}}$	$0.406 \pm 0.070$	$3.65 \pm 0.04$	
62	J033209.5–274807	−14.26	−0.04	20.87	19.63	0.12	0.91	0.89	$\sim 1^{\text{d}}$	$\sim 1^{\text{d}}$	$0.088 \pm 0.001$	$2.77 \pm 0.03$	
63	J033208.7–274735	−13.09	−0.49	19.21	17.86	0.15	0.93	0.88	$\sim 1^{\text{d}}$	$\sim 1^{\text{d}}$	$0.109 \pm 0.000$	$3.62 \pm 0.05$	
64	J033208.1–274658	−14.23	−0.31	25.32	24.27	0.14	0.02	0.01	...	...	$-0.056 \pm 0.090$	$2.27 \pm 0.04$	
66	J033203.7–274604	−13.94	+0.56	21.40	19.29	0.37	0.03	0.03	$0 < 0.016$	$0 < 0.011$	$0.032 \pm 0.006$	$3.32 \pm 0.03$	
67	J033202.5–274601	−13.99	−0.40	24.71	22.73	0.18	0.02	0.04	$0.35 < 0.49$	$0.46^{+0.018}_{-0.025}$	$0.101 \pm 0.037$	$3.15 \pm 0.03$	
78	J033230.1–274524	−14.50	−0.54	23.04	21.45	0.26	0.37	0.03	$0.655^{+0.027}_{-0.20}$	$0.357^{+0.008}_{-0.009}$	$0.233 \pm 0.021$	$3.24 \pm 0.02$	
81	J033226.0–274515	−15.04	−0.43	26.41	25.26	0.10	0.13	0.13	...	...	$-0.128 \pm 0.115$	$2.23 \pm 0.08$	
83	J033215.0–274225	−14.45	−0.22	23.80	22.01	0.25	0.03	0.03	$0 < 0.0499$	$0.0378 < 0.0544$	$0.096 \pm 0.032$	$3.13 \pm 0.03$	
86	J033233.9–274521	−15.16	−0.04	25.32	24.13	0.31	0.00	0.00	...	...	$0.102 \pm 0.202$	$2.71 \pm 0.05$	
89	J033208.3–274153	−14.97	−0.44	25.23	24.24	0.12	0.10	0.04	...	...	$0.068 \pm 0.068$	$2.63 \pm 0.07$	
149	J033212.3–274621	−15.02	+0.12	23.85	21.76	0.32	0.03	0.03	$0 < 0.064$	$0 < 0.088$	$0.114 \pm 0.043$	$2.77 \pm 0.02$	
155	J033208.0–274240	−14.88	+0.17	23.06	21.11	0.47	0.00	0.03	$0 < 0.0053$	$0 < 0.031$	$0.175 \pm 0.046$	$3.64 \pm 0.04$	
173	J033216.8–274327	$< -15.30$	−1.00	22.88	21.11	0.22	0.03	0.03	$0 < 0.026$	$0 < 0.043$	$0.115 \pm 0.011$	$2.67 \pm 0.02$	
185	J033211.0–274343	−15.19	+0.14	22.39	20.54	0.62	0.00	0.03	$0.026^{+0.0018}_{-0.0018}$	$0.024^{+0.0067}_{-0.0037}$	$0.466 \pm 0.056$	$2.20 \pm 0.02$	Truncated by chip edge
224	J033228.8–274621	$< -15.32$	−1.00	22.97	20.76	0.27	0.03	0.03	$0 < 0.018$	$0.084^{+0.013}_{-0.026}$	$0.060 \pm 0.014$	$3.28 \pm 0.03$	
266	J033214.0–274249	−14.88	+1.00	22.29	20.35	0.69	0.00	0.03	$0 < 0.0036$	$0 < 0.0036$	$0.148 \pm 0.045$	$3.32 \pm 0.01$	
515	J033232.2–274652	−14.90	+0.42	27.78	25.41	0.19	0.01	0.00	...	...	$-0.161 \pm 0.253$	$2.57 \pm 0.10$	
532	J033214.2–274231	−15.09	−0.05	24.81	23.64	0.13	0.22	0.04	$0.93^{+0.0056}_{-0.18}$	$0.58^{+0.12}_{-0.14}$	$0.126 \pm 0.042$	$3.20 \pm 0.07$	
535	J033211.5–274650	−14.89	+0.02	22.69	20.82	0.31	0.03	0.03	$0.013 < 0.11$	$0.12^{+0.012}_{-0.015}$	$0.110 \pm 0.017$	$3.24 \pm 0.03$	
536	J033210.9–274235	−15.16	−0.24	19.97	18.17	0.59	0.03	0.03	$0 < 0.0076$	$0 < 0.0086$	$0.099 \pm 0.005$	$3.13 \pm 0.02$	Double nucleus, $0''3$ sep.
538	J033208.6–274649	−15.10	+0.12	19.90	18.19	0.85	0.03	0.03	$0.00172 < 0.021$	$0.011 < 0.030$	$0.220 \pm 0.007$	$3.50 \pm 0.02$	Truncated by chip edge
560	J033206.3–274537	$< -15.33$	−1.00	23.05	20.65	0.27	0.03	0.03	$0 < 0.15$	$0.0068 < 0.061$	$0.059 \pm 0.012$	$3.34 \pm 0.03$	
563	J033231.5–274624	$< -15.34$	−1.00	23.64	22.31	0.26	0.02	0.03	$0.0067 < 0.13$	$0 < 0.076$	$0.641 \pm 0.045$	$3.07 \pm 0.03$	
593	J033214.8–274403	$< -15.34$	−1.00	26.27	24.51	0.47	0.00	0.00	...	...	$0.100 \pm 0.250$	$2.66 \pm 0.08$	
594	J033209.8–274249	$< -15.19$	−1.00	22.93	20.30	0.44	0.02	0.03	$0 < 0.0093$	$0.025^{+0.0033}_{-0.0032}$	$0.066 \pm 0.019$	$3.61 \pm 0.03$	
623	J033228.6–274659	$< -15.35$	−1.00	26.95	26.35	0.12	0.00	0.00	...	...	$0.156 \pm 0.236$	$1.75 \pm 0.65$	
624	J033229.3–274708	$< -15.33$	−1.00	22.68	20.36	0.33	0.03	0.03	$0 < 0.0060$	$0 < 0.012$	$0.034 \pm 0.013$	$3.46 \pm 0.03$	
626	J033209.5–274758	$< -15.33$	−1.00	25.44	24.20	0.21	0.01	0.00	...	...	$0.123 \pm 0.163$	$3.20 \pm 0.09$	
631	J033215.2–274335	$< -15.32$	−1.00	25.13	22.93	0.23	0.00	0.03	$0.027 < 0.10$	$0.054 < 0.099$	$0.038 \pm 0.065$	$2.80 \pm 0.04$	

<sup>a</sup>Sources detected only in CXO soft band (0.5–2 keV) indicated with upper limits

<sup>b</sup>X-ray hardness ratio  $\equiv (H - S)/(H + S)$ , for hard- and soft-band counts  $H$  and  $S$

<sup>c</sup>If 0 is not excluded at  $> 3\sigma$ , only  $3\sigma$  upper limit is shown; otherwise limits are  $\pm 1\sigma$ .

<sup>d</sup>HST-unresolved sources omitted from 2-D fitting, plotted with  $f_{\text{nuc}} \equiv f_{\text{tot}}$  in Fig. 4